Materials Science & Engineering A 885 (2023) 145650

Contents lists available at ScienceDirect

Materials Science & Engineering A

journal homepage: www.elsevier.com/locate/msea

Exceptional thermal stability of additively manufactured CoCrFeMnNi high-entropy alloy with cellular dislocation structures

Yanfang Liu [a,b], Jie Ren [b], Jian Liu [b], Yang Cao [a,**], Wei Liu [a], Tianyi Li [c], Yuntian Zhu [a,d], Wen Chen [b,*]

[a] Nano and Heterogeneous Materials Center, School of Materials Science and Engineering, Nanjing University of Science and Technology, Nanjing, 210094, China
[b] Department of Mechanical and Industrial Engineering, University of Massachusetts, Amherst, MA, 01003, USA
[c] X-ray Science Division, Argonne National Laboratory, Argonne, IL, 60439, USA
[d] Department of Materials Science and Engineering, City University of Hong Kong, Kowloon, Hong Kong, China

ARTICLE INFO

Keywords:
Additive manufacturing
High-entropy alloy
Thermal stability
Cellular dislocation structure
Precipitates

ABSTRACT

CoCrFeMnNi high-entropy alloy (HEA) was additively manufactured (AM) by laser powder-bed fusion (L-PBF). The AM CoCrFeMnNi has prominent cellular dislocation structures with a small number of Mn-rich oxides. The thermal stability of the AM CoCrFeMnNi was investigated by isochronal annealing treatment at various temperatures from 400 to 1300 °C for 1 h. Microstructural analysis shows slow dislocation recovery, retarded recrystallization process, and precipitation of additional Cr-Mn based oxides during thermal annealing, resulting in exceptional thermal stability and retained high hardness at elevated temperatures. By thermodynamic calculations, a low stored energy of 1.31 MJ/m^3 and a high activation energy of 353 kJ/mol for recrystallization were estimated for the AM CoCrFeMnNi. The exceptional thermal stability of the AM CoCrFeMnNi HEA is mechanistically attributed to the low crystallographic misorientations across the dislocation cell walls, sluggish atomic diffusion, and the pinning effects of the oxide nanoprecipitates.

1. Introduction

Laser powder-bed fusion (L-PBF) has been widely explored as one of the most promising additive manufacturing techniques for industrial applications due to the advantage of design freedom for complex geometries [1,2]. The far-from-equilibrium solidification conditions (e.g., large thermal gradients and high cooling rates) during L-PBF often result in hierarchical microstructures that consist of heterogeneous grain geometries, low-angle grain boundaries (LAGBs), and cellular dislocation structures [3–6]. The cellular dislocation structures refer to an array of dislocation cells with dislocation-free interiors and dislocation-rich cell walls. Such cellular dislocation structures in additively manufactured (AM) materials are different from the dislocation cells in metals processed by traditional cold working. Cold working creates sub-grain dislocation cells with a broad range of sizes and misorientation angles, and the resultant chemical segregation is usually negligible [7]. In contrast, the dislocation cells in AM materials usually possess thick cell walls that are often reinforced by Lomer locks and/or solidification-induced chemical segregation [1,8]. The crystallographic misorientations across the cell walls are generally low [8,9]. The distinct dislocation assembly in the cellular structures of AM materials promotes effective blockage and accumulation of dislocations for profound strengthening, and meanwhile helps stabilize strain hardening by enabling dislocation transmission across the cell walls at the later stage of plastic deformation [8,9]. As a result, many AM materials exhibit exceptional combinations of strength and ductility that surpass their conventional counterparts made by casting or thermomechanical treatment [6,10].

The rapid development of metal additive manufacturing is mainly driven by industrial needs and thus early research works have primarily focused on conventional alloys such as steels [1,3] and aluminum alloys [11–13]. High-entropy alloys (HEAs) are an emerging class of materials that has recently gained tremendous attention because of their excellent mechanical properties, such as high strength, ductility, and fracture toughness [14–18]. However, the thermal stability of many HEAs produced by casting or traditional thermomechanical processing is still

* Corresponding author.
** Corresponding author.
E-mail addresses: y.cao@njust.edu.cn (Y. Cao), wenchen@umass.edu (W. Chen).

https://doi.org/10.1016/j.msea.2023.145650
Received 15 July 2023; Received in revised form 30 August 2023; Accepted 31 August 2023
Available online 1 September 2023

disappointing, resulting in deterioration of mechanical properties over a wide temperature range of 500-900 °C [19,20]. Specifically, at intermediate temperatures, the entropy of mixing in HEAs often cannot overwrite the enthalpy of mixing, leading to metastable solid solution phases. Therefore, decomposition of the solid solution phases commonly occurs upon prolonged annealing, which promotes the formation of brittle intermetallics or nanoclusters at grain boundaries and causes undesired ductility loss [19,21]. At high temperatures, grain growth and dislocation annihilation result in a rapid decrease in the strength of many HEAs [19,20]. Considering the unique feature of solidification cellular structures in AM materials, it is expected that the microstructural evolution in AM HEAs upon thermal exposure can be different from that in the traditionally processed HEA counterparts [22]. Moreover, from a practical viewpoint, a fundamental understanding of the microstructural evolution and mechanical properties upon thermal exposure is critically needed for the direct deployment of AM HEAs for applications under extreme environments.

In this work, taking the AM CoCrFeMnNi HEA as a model system, we study its thermal stability over a broad range of temperatures from 400 to 1300 °C. CoCrFeMnNi, also called Cantor alloy [23], has been widely studied due to its outstanding mechanical properties at both ambient and cryogenic temperatures [15,24]. Recently, we have shown that AM CoCrFeMnNi exhibits prominent cellular dislocation structures that give rise to superior mechanical properties compared to their as-cast counterparts [6]. Here, we reveal slow dislocation recovery, retarded recrystallization process, and precipitation of nanoscale oxides during thermal annealing, resulting in exceptional thermal stability and retained high hardness at elevated temperatures. The high thermal stability of the AM CoCrFeMnNi HEA is mechanistically attributed to the low crystallographic misorientations across the dislocation cell walls, sluggish atomic diffusion, and the pinning effects of the oxide nanoprecipitates. Our finding has a broad ramification for the development of thermally stable metallic alloys for high-temperature applications by additive manufacturing.

2. Methods

The L-PBF CoCrFeMnNi samples were fabricated by an EOS M290 system with the laser beam size of 100 μm. Gas-atomized CoCrFeMnNi powders with particle sizes ranging from 15 to 53 μm were used. The samples were deposited onto a high-strength 4340 steel substrate by the bi-directional and cross-hatched scan strategy, as shown in Fig. 1a. During L-PBF processing, the substrate was pre-heated to 80 °C to minimize thermal residual stresses. The processing chamber was filled with high-purity argon gas and the oxygen content was maintained below 10 ppm during printing. To obtain samples without printing

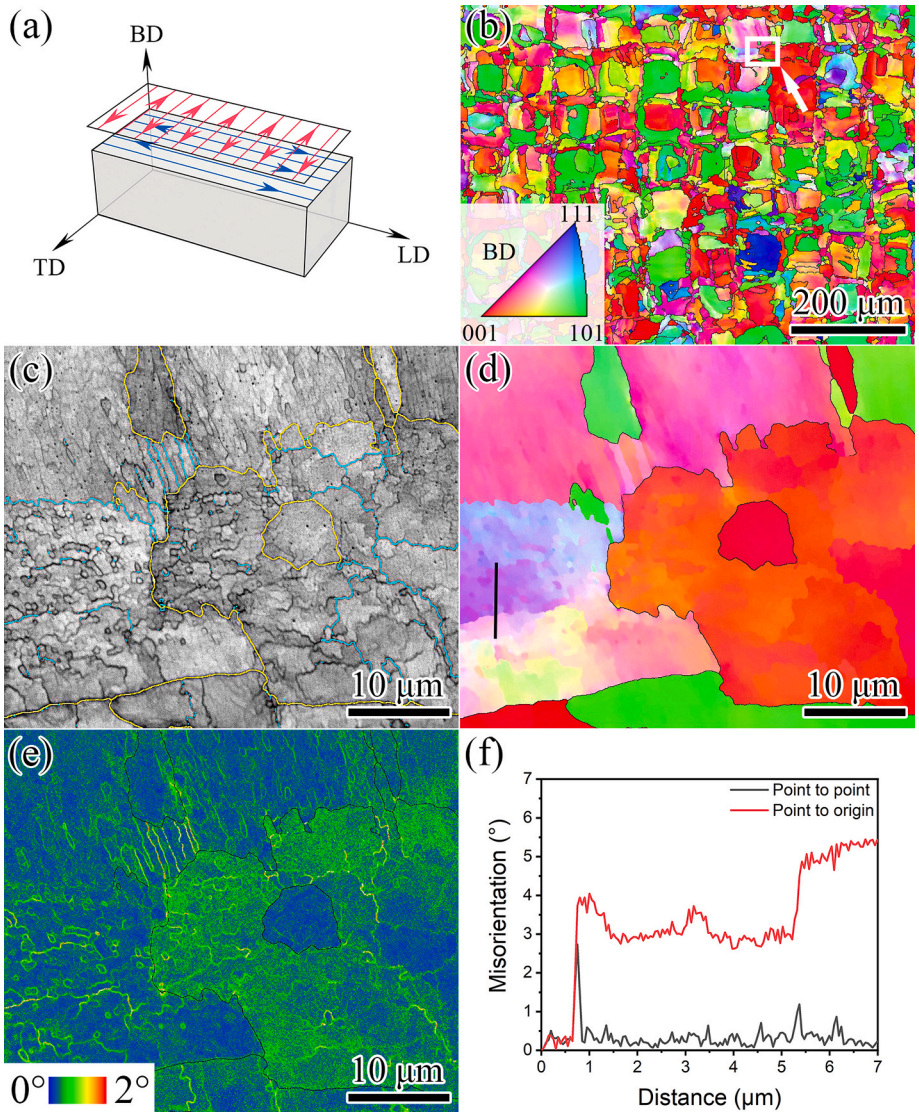

Fig. 1. (a) Schematic illustration of the bi-directional and cross-hatched scan strategy for fabricating the L-PBF CoCrFeMnNi HEA. BD: build direction, LD: longitudinal direction, TD: transverse direction; (b) An EBSD map showing the microstructure on the LD-TD plane of the as-printed sample; (c), (d), and (e) are the image-quality (IQ), IPF, and KAM maps extracted from the white-square region in (b), respectively, showing details of cellular and columnar structures; (f) Plots of the correlated and uncorrelated misorientation angles measured along the black lines sketched in (d).

defects such as keyholes or lack-of-fusion, a density optimization approach was performed, as elaborated in our prior work [6,25,26]. The optimized processing condition of 250 W laser power and 1000 mm/s scan speed was selected for fabricating near fully-dense samples (99.7% relative density). To study their thermal stability, the printed samples were isochronally annealed for 1 h at different temperatures ranging from 400 to 1300 °C in a tube furnace, follow by water quenching.

The relative density of the as-printed CoCrFeMnNi samples was measured by an AccuPyc II 1340 gas pycnometer. The phase and microstructure in the longitudinal direction (LD)- transverse direction (TD) planes were analyzed by high-energy synchrotron X-ray diffraction (SXRD), electron backscatter diffraction (EBSD), energy dispersive spectroscopy (EDS), and transmission electron microscopy (TEM). Samples for SXRD, EBSD and EDS analyses were first mechanically polished by SiC abrasive papers down to 1500 grit size and further polished using OP-U and OP-S solutions to remove strained surface layer. TEM samples were prepared by first grinding to a thickness of ~60 μm, followed by electro-polishing in an electrolyte of 20% nitric acid and 80% methanol with an operating voltage of 40-50 V at the temperature of -40 °C until a central perforation was achieved. SXRD measurements were performed at the beamline 11-ID-C at the Advanced Photon Source (APS), Argonne National Laboratory (ANL). A monochromatic X-ray beam with an energy of 105.7 keV and a wavelength of 0.1173 Å was used. EBSD analyses were performed using a Zeiss Auriga scanning electron microscope (SEM) equipped with EDS. TEM experiments were carried out on a TECNAI-G2-20-LaB6 microscope operating at 200 kV. Vickers hardness was measured on the polished LD-TD surface using an HMV-G21DT indentation equipment with an applied load of 980.7 mN and a dwell time of 15 s for each indentation. The distance between neighboring indents was at least 200 μm to avoid overlaps of strain fields.

3. Results

3.1. As-printed microstructure

Fig. 1a shows the schematic illustration of the bi-directional and cross-hatched scan strategy for fabricating the L-PBF CoCrFeMnNi HEA. EBSD analyses were conducted to investigate the microstructures of the as-printed sample. Fig. 1b-e shows the top-view microstructure perpendicular to the build direction (BD) of the as-printed sample. The inverse pole figure (IPF) image in Fig. 1b shows the typical “chess board” pattern, which is attributed to the 90° rotation of the laser scanning tracks between adjacent layers, as shown by the red and blue arrows in Fig. 1a. The black lines delineate the high-angle grain boundaries (HAGBs) with misorientation angles larger than 15°. Most of the small grains are located on the “frames of the board” while the large grains are inside the “frames”. Fig. 1c-d shows the enlarged images of the area enclosed by the white square in Fig. 1b. Both cellular and columnar structures were observed (Fig. 1c). It has been reported that the cellular structures in L-PBF alloys are largely due to constitutional-supercooling-induced cellular solidification mode combined with thermal-cycling-induced cellular dislocation structures [8]. For a clear view, LAGBs with misorientation angles of 2-15° are traced by olive lines, and the HAGBs are traced by yellow lines (Fig. 1c). Notably, a small percentage of cell walls overlaps with LAGBs, likely due to dislocation recovery during L-PBF. Change in contrast between the cellular structures shown in Fig. 1d indicates the existence of local strain gradients, which is induced by the accumulation of geometrically necessary dislocations (GNDs) at the cell walls. This is also confirmed by the kernel average misorientation (KAM) analysis in Fig. 1e. The misorientation angle distribution along the black line in Fig. 1d is shown in Fig. 1f. It is seen that the misorientation angles across the intragranular solidification cell walls are well below 1°. Such intercellular misorientation angles in AM materials seem substantially lower than those across the dislocation walls in conventional plastically-deformed samples (>1.5°) [27].

Fig. 2a shows the typical cellular dislocation structures in the AM CoCrFeMnNi. The dislocation cells are equiaxed with an average size of ~420 nm. The majority of the dislocations aggregate at the cell walls. EDS analysis reveals uniform elemental distributions with no significant chemical segregation, as shown in Fig. 2b. The chemical homogeneity arises presumably due to the high cooling rate that effectively suppresses atomic diffusion during L-PBF. Nonetheless, precipitates of a few tens of nanometers are visible. High resolution EDS mapping confirms that these nanoscale precipitates are Mn-rich oxides, as illustrated in Fig. 2c [4,28].

3.2. Mechanical properties after annealing treatment

Microhardness tests were carried out to investigate the thermal stability of the L-PBF CoCrFeMnNi HEA. Fig. 3a shows the microhardness values of the L-PBF samples annealed at different temperatures for 1 h. The average hardness of ~239 HV for the as-printed L-PBF sample is marked by the red dashed line. The hardness increases slightly up to ~250 HV after annealing at 500 °C, thereafter it decreases gradually with increasing annealing temperatures up to 1300 °C. A moderate hardness increase after annealing at 400 - 600 °C may be caused by the annealing-induced hardening effect [29,30]. The cold-worked CoCrFeMnNi HEAs produced via high-pressure torsion (HPT), cold rolling (CR), equal-channel angular pressing (ECAP) [19,31,32], also show a similar annealing-induced hardening effect at low temperatures (Fig. 3b). It has been reported that the formation of long-range ordered structure and/or the reduced mobile dislocation density are possibly responsible for such abnormal annealing-induced hardening effect at low temperatures [33,34]. As the annealing temperature increases from 500 to 1300 °C, the hardness of the L-PBF sample gradually decreases due to dislocation recovery and recrystallization, to be discussed later. At this temperature regime, the relative percentage of the hardness drop in the L-PBF sample is much smaller than those in the conventional cold-worked counterparts. Although the cold-worked samples are harder than the L-PBF sample at low temperatures, the hardness of the L-PBF sample is much higher than those of conventional counterparts at high temperatures above 900 °C, leading to a cross-over in the hardness-temperature plot. Such exceptional thermal stability of the L-PBF sample is more clearly revealed by the normalized hardness plot as a function of temperature shown in Fig. 3c.

3.3. Microstructure after isochronal annealing

Fig. 4 shows the SXRD patterns of the L-PBF samples after annealing treatment. The face-centered cubic (FCC) structure was retained over the entire annealing temperature range (Fig. 4a). The dislocation density was calculated by the modified Williamson-Hall (MWH) method [35], which considers the average sub-grain (crystallite) size D and the strain effects, based on the SXRD peak broadening as follows:

$$(\Delta K)^2 = \left(\frac{0.9}{D}\right)^2 + \left(\frac{\pi A^2 b^2 \rho}{2}\right)\left(K^2\overline{C}\right) + O\left(K^2\overline{C}\right)^2 \quad (1)$$

where $K = 1/d$, $\Delta K = -K(\Delta d/d)$, d is the interplanar spacing, Δd the full width at half maximum of the diffraction peak, b the Burgers vector, and ρ the dislocation density; A is the dislocation distribution parameter that depends on the effective outer cut-off radius of dislocations, and it is usually 1 ~ 2 [36]; O is the non-interpreted high order term of $K^2\ \overline{C}$. Under the assumption that all possible slip systems are equally populated, the (hkl)-dependent average dislocation contrast factor $\overline{C}$, is given by:

$$\overline{C} = \overline{C}_{h00}\left(1 - qH^2\right) \quad (2)$$

where $H^2 = (h^2k^2 + k^2l^2 + h^2l^2)/(h^2 + k^2 + l^2)^2$, and $\overline{C}_{h00}$ is the average dislocation contrast factor for ($h00$) reflections and related to the type of

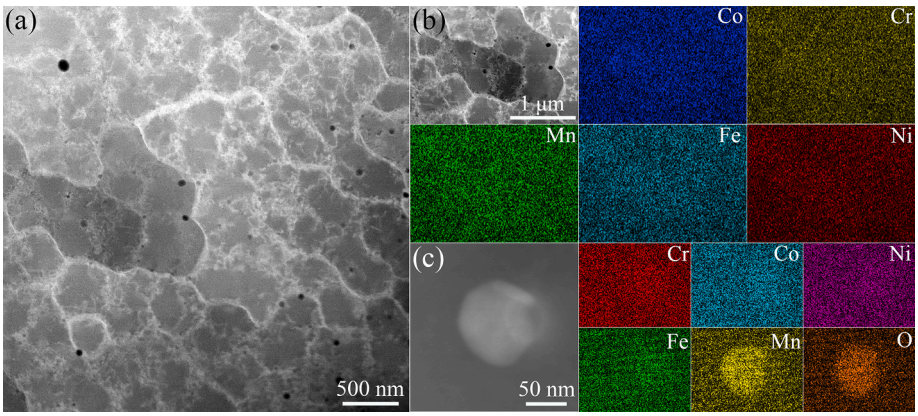

Fig. 2. (a) STEM/HAADF image showing typical cellular dislocation structures in the as-printed sample; (b) STEM-EDS elemental maps of the cellular dislocation structures; (c) STEM-EDS elemental maps of a precipitate.

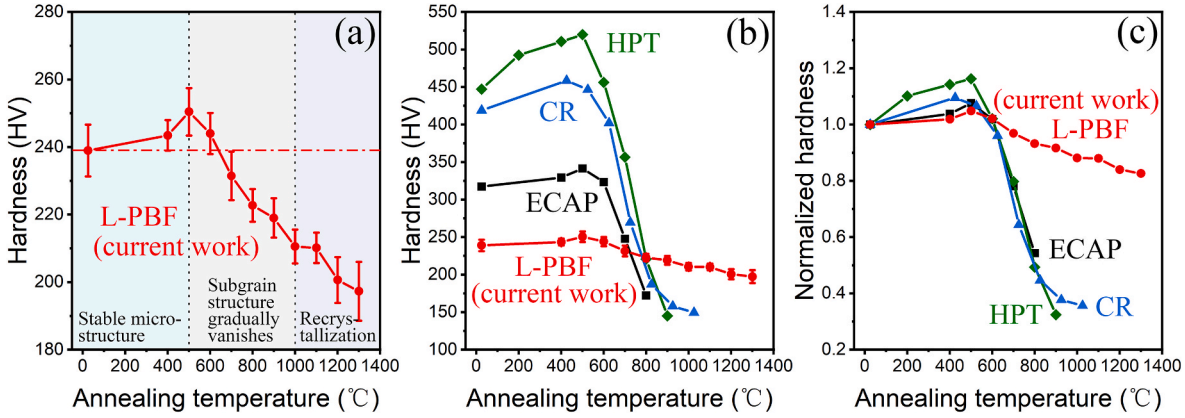

Fig. 3. (a) Hardness evolution with respect to the annealing temperature for the L-PBF CoCrFeMnNi HEAs; (b) Comparison of hardness evolution with respect to varying annealing temperatures between the L-PBF sample and the cold-worked samples produced via HPT, CR, and ECAP; (c) Comparison of normalized hardness with respect to varying annealing temperatures. Normalized hardness is defined as: HV/HV_0, where HV is the hardness value at different temperatures and HV_0 is the hardness value before annealing treatment.

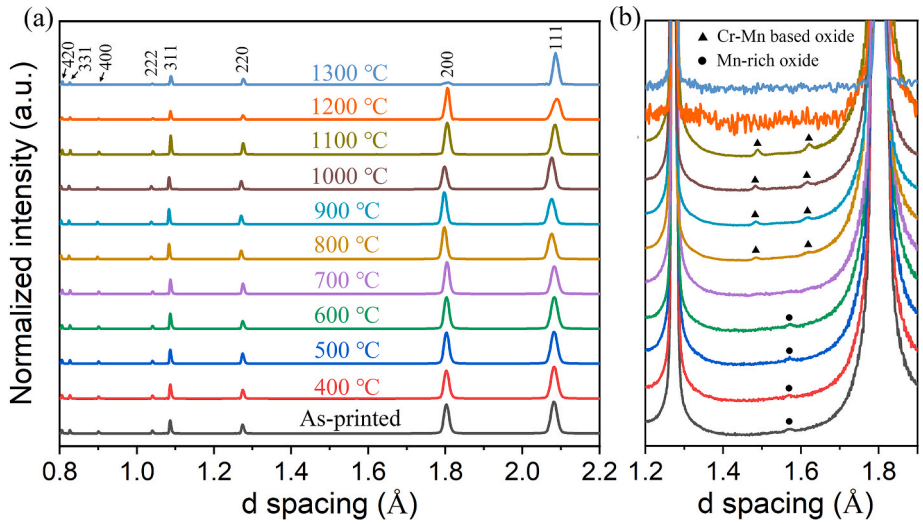

Fig. 4. (a) SXRD patterns of the as-printed and annealed samples; (b) Enlarged diffraction patterns with d-spacing ranging from 1.2 to 1.9 Å, showing the existence of oxide phases.

dislocations and anisotropic elastic constants C_{11}, C_{12}, and C_{44}. The values of $C_{11} = 172.1$ GPa, $C_{12} = 107.5$ GPa and $C_{44} = 92$ GPa are used for calculation [37]. q is a variable related to the fractions of screw and edge dislocations, which can be experimentally determined by the least square linear regression of $[(\Delta K)^2 - (0.9/D)^2]/K^2$ versus H^2. From the linear relationship of the modified Williamson-Hall plot, the slope m can

be obtained. Dislocation density ρ was calculated from the relation $\rho = 2m/\pi A^2 b^2$. As summarized in Table 1, the dislocation density gradually decreases from 3.5×10^{14} m^{-2} at as-printed state to 3.1×10^{14} m^{-2} after 500 °C annealing, then rapidly decreases to 1.3×10^{14} m^{-2} after 900 °C annealing, and eventually drops to 0.9×10^{14} m^{-2} after 1200 °C annealing. As mentioned earlier, the reduced numbers of mobile dislocations and dislocation sources lead to annealing-induced hardening upon annealing at 500 °C. Small amounts of oxides are also detected in both as-printed and annealed samples, as shown in Fig. 4b. The peaks marked with circles with the main peak at d-spacing ≈ 1.56 Å are related to the formation of Mn-rich oxides during additive manufacturing. After annealing at the temperature between 800 °C and 1100 °C, the new peaks marked with triangles appear with the main peaks at d-spacing ≈ 1.48 Å and 1.61 Å. The positions of new peaks are in good agreement with the Cr-Mn based oxides reported earlier in the literature [38].

The microstructures of the annealed L-PBF samples were characterized by EBSD. Fig. 5 illustrates the IPF maps and the corresponding KAM maps of the samples annealed in the temperature range between 500 °C and 1300 °C. The EBSD step size was 1 μm. At this length scale, the "chess board" patterns remain stable up to 1100 °C. The recrystallized grains with low strains are distinguished by low KAM values and appear blue. The recrystallized grains start to form at 1000 °C (Fig. 5m). With increasing the annealing temperature, the volume fraction of the recrystallized grains increases. The coexistence of cellular structures and recrystallized grains is found in the 1200 °C-annealed sample (Fig. 5o). The recrystallized grains are preferentially distributed at the boundaries of the "chess board" grains. Full recrystallization is eventually reached after 1300 °C annealing. Apparently, the temperature to achieve a near defect-free microstructure for the L-PBF CoCrFeMnNi is well above the recrystallization temperature (800 °C) of the conventional counterpart produced by ECAP [32].

Fig. 6 demonstrates quantitative analysis of the microstructural evolution at different annealing temperatures, based on the EBSD data. The average grain size (defined by HAGBs) increases slightly from ~13 to ~16 μm as the annealing temperature rises to 1100 °C, and meanwhile the fraction of LAGBs is largely retained at ~50% (Fig. 6a). Above 1100 °C, the average grain size rapidly increases to ~64 μm and the LAGB fraction sharply decreases from ~50% to ~3% due to vigorous recrystallization (Fig. 6a). In examining the distributions of misorientation angles for the as-printed and annealed samples, Σ3 annealing twin boundaries with 60° misorientation are found in the samples annealed at temperatures of 1000 °C and above. Annealing twins are part of the recrystallization behavior shown in Figs. 5 and 6b. To capture microstructures of different feature sizes during the EBSD experiments, both 1 μm and 0.2 μm step sizes were used to analyze the local misorientations (Fig. 6c). At annealing temperatures below 1100 °C, the two sets of local misorientation data measured with different step sizes follow a similar trend in distribution (Fig. 6c and d). Above 1100 °C, the sharp decline in local misorientation (Fig. 6c) is consistent with the substantial drop in the volume fraction of LAGBs (Fig. 6a), which is caused by the consumption of strain energy and depletion of the surrounding sub-grain structures at such high temperatures.

Table 1
Microstructural characteristics of the L-PBF CoCrFeMnNi HEAs after annealing at different temperatures (LAGB fraction f_{LAGBs}, local misorientation angle θ_{local}, measured by 0.2 μm step size, grain size defined by HAGBs, area fraction of recrystallized grains X_a).

	ρ (10^{14} m^{-2})	f_{LAGBs} (%)	θ_{local} (°)	Grain size (μm)	X_a
As-printed	3.5	52.8	0.43	13.7	
500 °C	3.1	53.8	0.44	13.1	
700 °C	2.1	51.8	0.44	15.3	
900 °C	1.3	50.3	0.38	13.7	
1000 °C	1.3	50.2		15.9	0.005
1100 °C	1.2	52.4	0.40	16.2	0.045
1200 °C	0.9	39.1		22.6	0.255
1300 °C		3.1		63.7	0.962

TEM analysis was also conducted to characterize the microstructural evolution after annealing at different temperatures (Fig. 7). The cellular structures comprising equiaxed dislocation cells are homogeneously distributed in the as-printed sample (Fig. 7a and b). Annealing at 500 °C for 1 h caused little change to the cellular structures (Fig. 7c and d). After annealing at 700 °C for 1 h, cell walls become thinner, but the cellular structures remain the overall shape (Fig. 7e and f). At 900 °C, some dislocation walls are disentangled while the remaining dislocation walls sharpen and transform into low angle boundaries via dislocation rearrangement and annihilation (Fig. 7g and h). With increasing the annealing temperature to 1100 °C, pronounced dislocation recovery results in the formation of stable sub-grains (Fig. 7i). Tilt boundaries comprising long arrays of dislocations are visible (Fig. 7j). This kind of tilt boundary is frequently found in metallic materials underwent strong recovery and polygonization [39]. Moreover, some newly formed precipitates are detected (Fig. 7g and i). This observation is consistent with the SXRD results shown in Fig. 4b.

Fig. 8a and b shows the microstructures after annealing at 1100 °C for 1 h. The microstructure is comparatively heterogeneous that some grains contain dislocation cells while some grains are free of dislocation cells. Rectangular precipitates are seen at the grain boundaries. EDS analysis on the enclosed area in Fig. 8b confirms that these precipitates are Cr-Mn based oxides (Fig. 8c). However, there is no apparent chemical segregation at the grain boundaries. According to the literature [40], Mn-rich oxides prefer to absorb Cr atoms, while repelling other elements at the grain boundaries. These oxides can impose strong pinning effects on dislocation motion and grain boundary migration, and thus retard the recrystallization process [41].

4. Discussion

4.1. Stored energy

In order to explore the thermodynamic origin of the enhanced thermal stability of the L-PBF CoCrFeMnNi, we calculated the stored energies due to dislocations (E_ρ) and boundaries (E_b), based on the microstructural analysis and thermophysical data from the literatures [42,43]. The stored energy contributed by dislocations can be estimated by Ref. [44]:

$$E_\rho = \frac{1}{2}\rho G b^2 \tag{3}$$

where G is the shear modulus. For the CoCrFeMnNi HEA, the values of G and b are taken as 80 GPa and 0.254 nm, respectively [42]. ρ in the as-printed sample is measured to be 3.5×10^{14} m^{-2} (Table 1). Then, E_ρ of 0.9 MJ/m^3 (31.4 J/mol) is calculated and collected in Table 2.

The stored energy due to grain and sub-grain boundaries can be estimated by Ref. [45]:

$$E_b = \gamma_{GB} S_v \tag{4}$$

where, γ_{GB} is the average boundary energy, S_v the equivalent boundary area per unit volume. The γ_{GB} value can be calculated by Refs. [45,46]:

$$\gamma_{GB} = \sum_{2^\circ}^{63.5^\circ} [\gamma(\theta) f(\theta)] \tag{5}$$

where, $f(\theta)$ is the boundary fraction, which can be retrieved directly from the EBSD data. $\gamma(\theta)$ is a function of misorientation θ across the boundaries, which is governed by the Read-Shockley relationship [47]:

$$\gamma(\theta) = \begin{cases} \gamma_S \dfrac{\theta}{15}\left[1 - \ln\left(\dfrac{\theta}{15}\right)\right], \theta \le 15^\circ \\ \gamma_S, \theta > 15^\circ \end{cases} \tag{6}$$

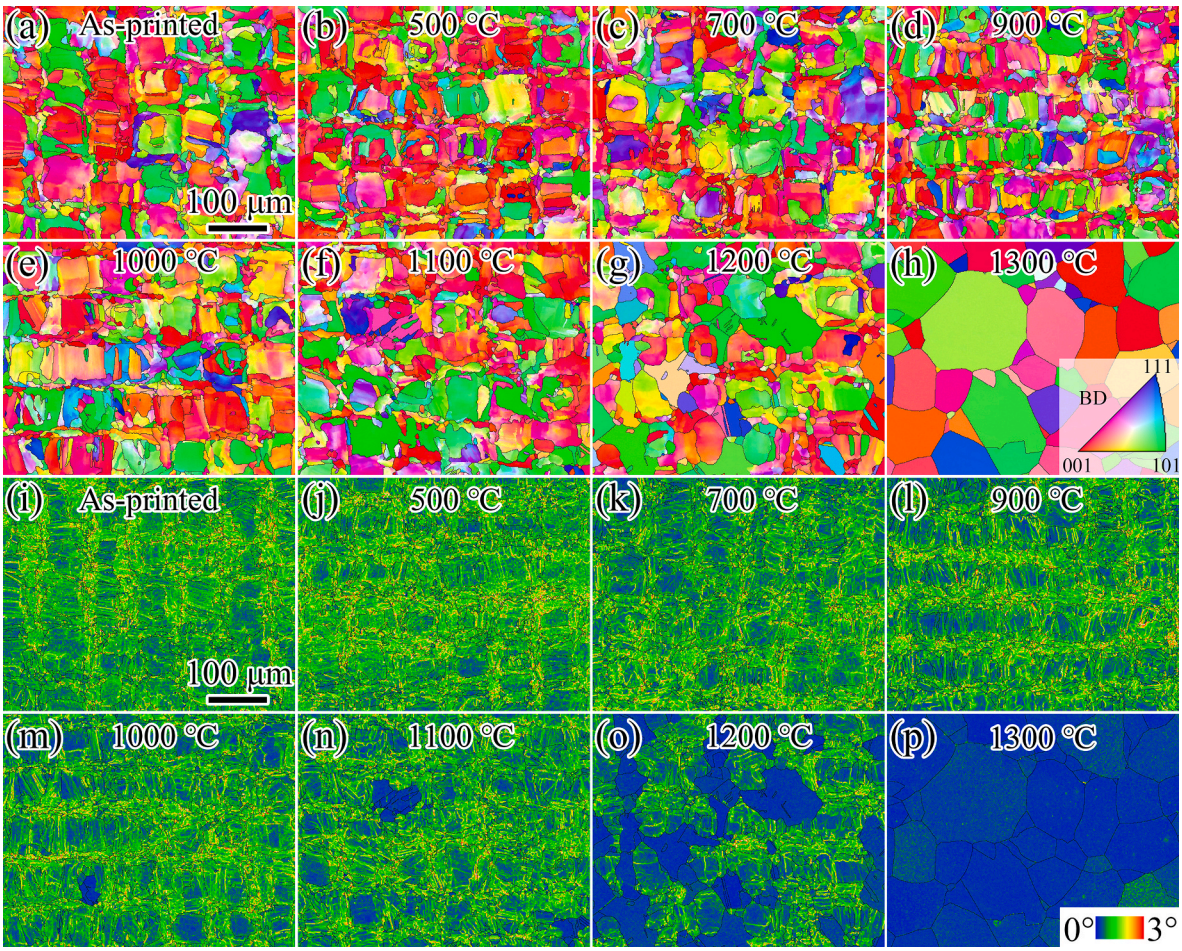

Fig. 5. Microstructures of the as-printed and annealed samples. The annealing temperature is provided in each image. (a)-(h) IPF maps; (i)-(p) KAM maps.

where $\gamma_S \approx 0.58\, J/m^2$ is the energy per unit area of a high-angle boundary for the CoCrFeMnNi HEA [43]; The S_v value for equiaxed sub-grains can be estimated by Ref. [48]:

$$S_v = \frac{3}{d_S} \tag{7}$$

where d_S is the sub-grain size, which can be measured from TEM images. Through Eq. (4) to **(7)**, E_b is calculated to be 0.41 MJ/m^3 (14.32 J/mol), and collected in Table 2.

The total stored energy in the bulk material is the sum of E_ρ and E_b, and is calculated to be 1.31 MJ/m^3. The total stored energy is the highest in the as-printed sample and decreases with increasing the annealing temperature. The stored energy due to dislocations is significantly higher than that due to grain and sub-grain boundaries, suggesting that significant recovery is necessary for effective energy reduction. The total driving pressure of 1.31 MPa, which is provided by the stored energy (i.e., 1.31 MJ/m^3), in the L-PBF CoCrFeMnNi is significantly smaller than that in plastically deformed metals, for example 14-24 MPa for severe-plastically-deformed nickel [49]. The very low stored energy contributes to the excellent thermal stability of the L-PBF CoCrFeMnNi HEA.

4.2. Recrystallization kinetics

In order to understand the kinetic mechanisms activated by thermal annealing, the activation energy for recrystallization is calculated based on the classical Johnson–Mehl–Avrami–Kolmogorov (JMAK) model [50]:

$$X_v = 1 - exp\,(-Bt^n) \tag{8}$$

Where X_v is the total volume fraction of recrystallized grains, B a temperature dependent parameter, t the annealing time in seconds, and n the JMAK exponent. Assuming that the recrystallized grains tend to be equiaxed, the area fraction X_a of recrystallized grains derived from EBSD (given in Table 1) is used to replace X_v in Eq. (8). Based on the Arrhenius law, B is calculated by:

$$B = B_0 \exp\left(-\frac{Q_r}{RT}\right) \tag{9}$$

where B_0 is a temperature-independent constant, Q_r the activation energy for recrystallization, T the absolute annealing temperature, and R the gas constant (8.314 J/(mol·K)). By substituting Eq. (9) into Eq. (8), the following relationship is obtained:

$$ln\left(ln\frac{1}{1-X_a}\right) - nlnt = ln\,B_0 - \frac{Q_r}{RT} \tag{10}$$

The term $ln\,[ln\,(1/1-X_a)]$ for isochronal annealing is plotted against $1/T$ for the L-PBF CoCrFeMnNi HEA, as shown in Fig. 9. Then the activation energy Q_r for recrystallization is equal to the slope of the linear fitting line drawn with the least square method.

The kinetics of recrystallization depends on the activation energy that is related to elemental self-diffusion and grain boundary diffusion. For the CoCrFeMnNi HEA, the activation energy for grain boundary diffusion of the constituting elements is in the range of 180.6-221.0 kJ/mol [43], and the activation energy for self-diffusion is in the range of 270-313 kJ/mol [51]. The L-PBF CoCrFeMnNi HEA has an activation energy of 353 kJ/mol for recrystallization (Fig. 9), which is much larger than that for elemental self-diffusion and grain boundary diffusion, and

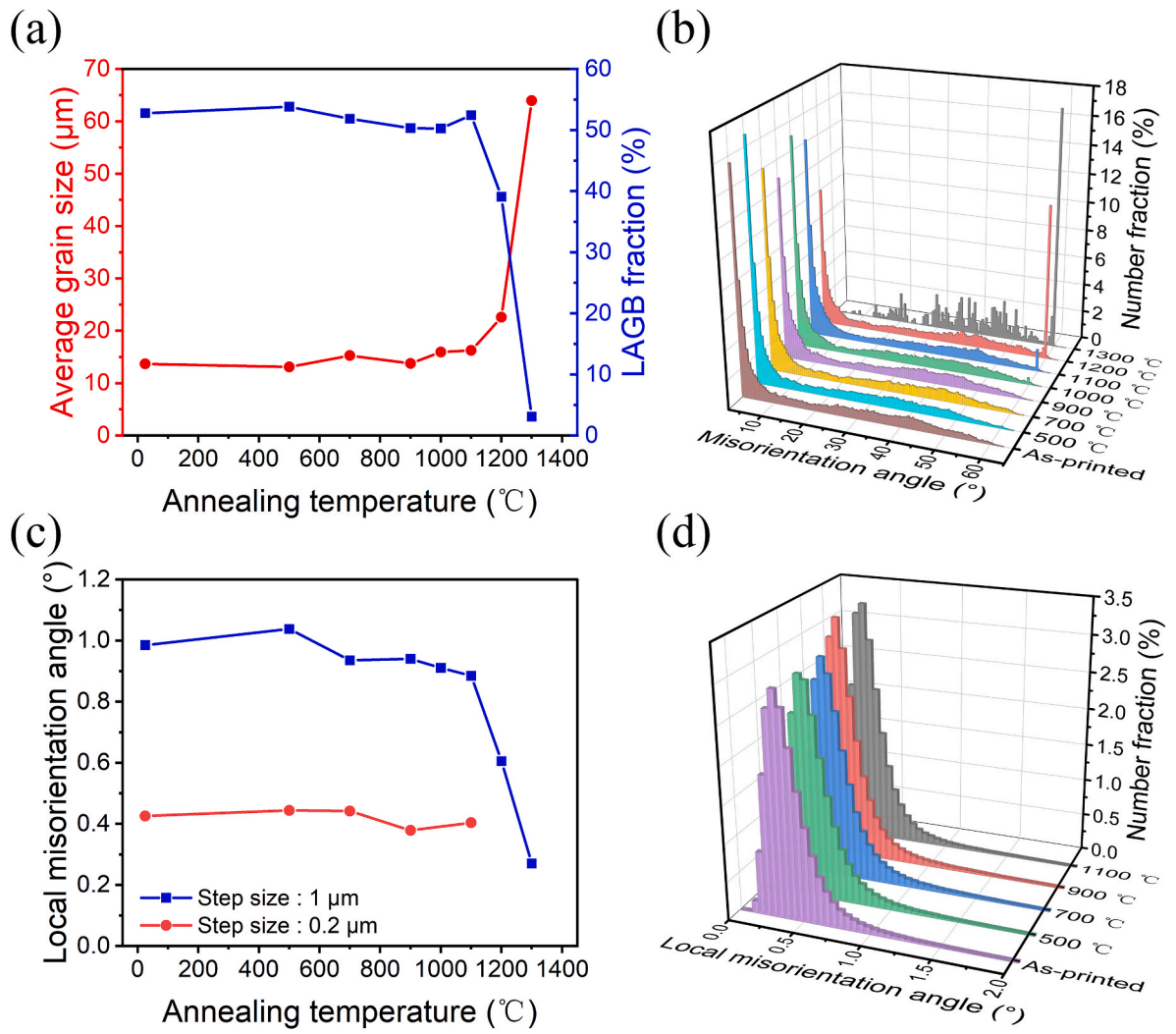

Fig. 6. (a) Changes in grain size and LAGB fraction with respect to annealing temperature; (b) Misorientation angle distributions with respect to annealing temperature; (c) Changes in local misorientation angle with respect to annealing temperature; Different step sizes were used for EBSD analysis; (d) Local misorientation angle distributions exported by 0.2 μm step size at different annealing temperatures.

also higher than the activation energy for recrystallization of many plastically deformed metal alloys such as cold-rolled Fe–Mn–C alloy (~230 kJ/mol) [52] and TWIP steels (~229 kJ/mol) [53]. It is known that HEAs have much higher activation energies for diffusion than pure metals because of the strong solute drag effect [54]. In addition, the pinning effects of the nanoscale precipitates also raise the activation energy for diffusion [41]. Therefore, the high activation energy for recrystallization of the L-PBF CoCrFeMnNi HEA is caused by the combined effect of sluggish elemental self-diffusion, sluggish grain boundary diffusion, low stored energy, and existence of nanoprecipitates.

4.3. Annealing behavior

Based on the dynamic variations in hardness and microstructure, the microstructural evolution with the increased annealing temperatures of the L-PBF CoCrFeMnNi can be divided into three stages, as shown earlier in Fig. 3a. At stage 1, when the annealing temperature rises to 500 °C, the microstructure remains highly stable with a subtle decrease in dislocation density from 3.5×10^{14} to 3.1×10^{14} m^{-2} (Fig. 7c and d and Table 1), indicating occurrence of slight recovery at this stage. Since the number of dislocation sources are reduced due to dislocation recovery, a higher stress is required to activate new dislocation sources to accommodate deformation, leading to the annealing-induced hardening phenomenon (Fig. 3a). In addition, Gu et al. [33] suggested that the formation of long-range ordered structure is also responsible for the annealing-induced hardening effect in the CoCrFeMnNi HEA. However, there is a lack of strong evidence of long-range ordered structure in our case.

At stage 2 at annealing temperatures of 500 – 1000 °C, sub-grain structures gradually vanish with the dislocation density rapidly decreasing from 3.1×10^{14} to 1.3×10^{14} m^{-2}, resulting in significant drops in hardness, even though newly formed precipitates appear at annealing temperature above 800 °C. The fraction of LAGBs and the average grain size are essentially unchanged. When the annealing temperature is raised to 1000 °C, ~58% reduction of dislocation density is achieved mainly by recovery, as shown in Fig. 5e and **m**. It is known that recovery and recrystallization compete with each other during annealing to consume stored strain energy [39]. By examining the microstructures of the annealed samples as shown in Fig. 5j to **m**, it is noted that the recovery event prevails during annealing at temperatures below 1000 °C while recrystallization is largely retarded since a significant amount of stored energy has been consumed by recovery at this stage.

At stage 3 at annealing temperatures higher than 1000 °C, newly stable sub-grain structures start to reconstruct and recrystallization sets in. For these annealed samples, there is a mixture of dislocation cell-free grains and dislocation cell-containing grains. It is difficult to justify the

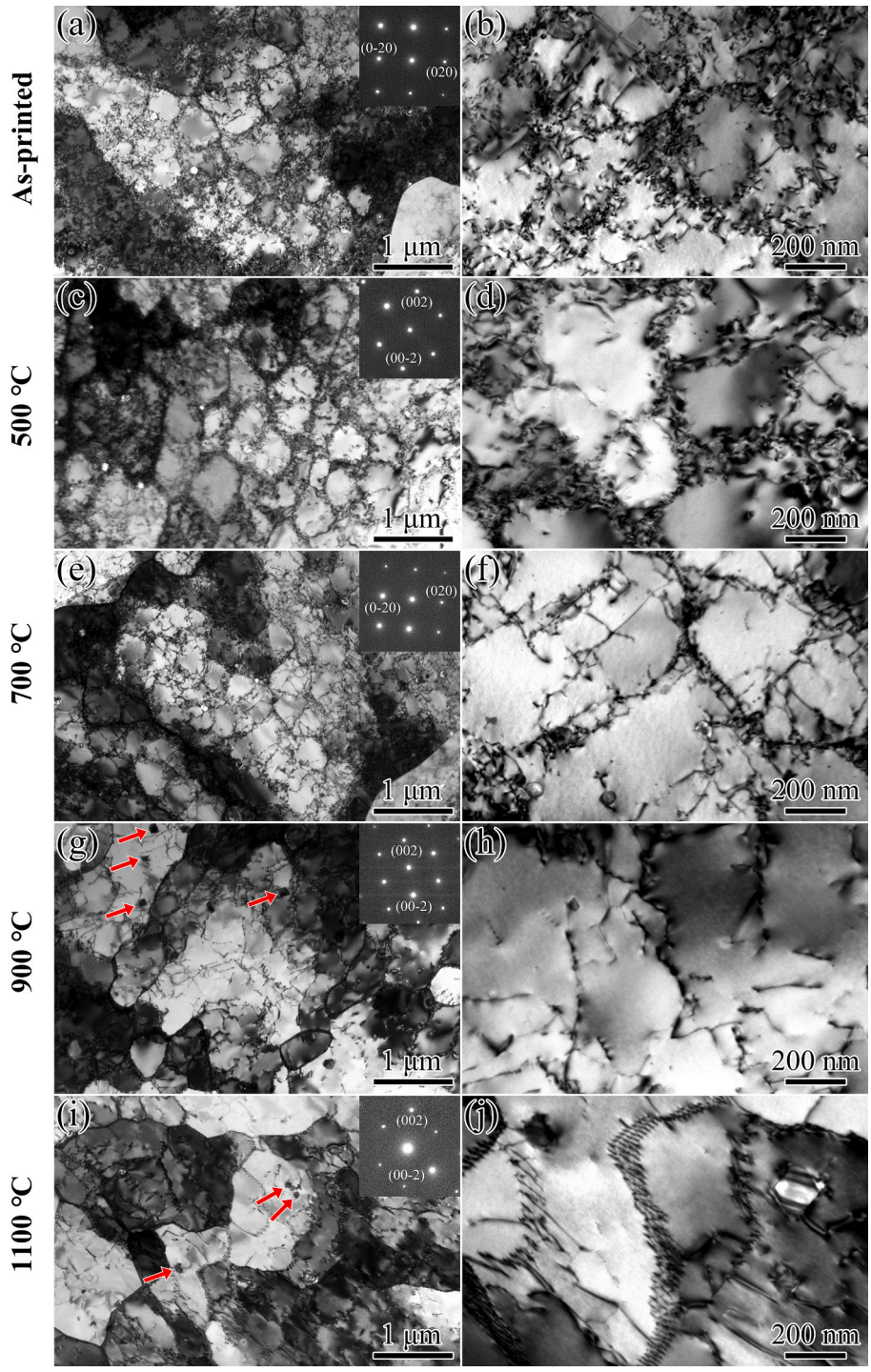

Fig. 7. TEM images showing microstructures in the (a, b) as-printed sample; (c, d) 500 °C annealed sample; (e, f) 700 °C annealed sample; (g, h) 900 °C annealed sample; and (i, j) 1100 °C annealed sample. Precipitates are marked by the red arrows in (g) and (i). (For interpretation of the references to colour in this figure legend, the reader is referred to the Web version of this article.)

overall predominance of recovery over recrystallization, but it is still reasonable to assume that at microscale the cells have to be decomposed and recovered before recrystallization can proceed since it is difficult for a grain boundary to migrate across a bunch of low-energy dislocation cells [55]. The recovery and recrystallization behaviors of the L-PBF CoCrFeMnNi HEA stand in contrast to those of the cold-worked CoCrFeMnNi HEAs that underwent pronounced recrystallization at much lower temperatures of 600 – 900 °C [32,56]. This difference arises from the fact that the cold-worked materials often possess significantly higher stored energy due to smaller grains, higher fractions of HAGBs, and higher dislocation densities, resulting in comparatively lower recrystallization temperatures. Moreover, cold-worked materials, especially materials produced by SPD, contain many defect-free crystals surrounded by mobile HAGBs [57,58]. These defect-free crystals are readily available recrystallization nuclei which are on the other hand unavailable in the L-PBF CoCrFeMnNi HEA. In addition to the unique architecture of cellular dislocation structures and the lack of recrystallization nuclei discussed above, the sluggish diffusion and strong pinning effects of nanoscale oxides/precipitates on dislocation motion and grain boundary migration also expectedly contribute to the enhanced

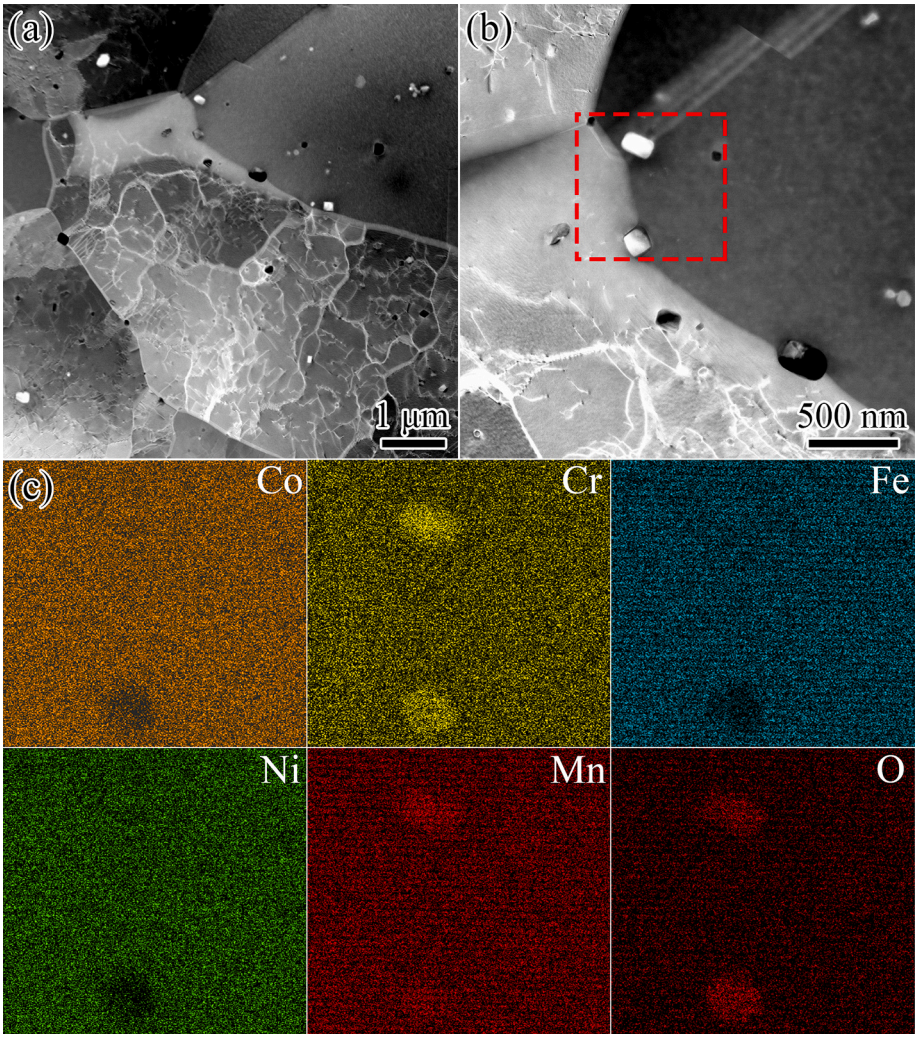

Fig. 8. STEM/HAADF images showing typical (a) grains and sub-grain cells and (b) precipitates in the sample annealed at 1100 °C; (c) EDS elemental maps for the local region illustrated by the dashed square box in (b).

Table 2
Structural parameters and stored energies in the L-PBF CoCrFeMnNi HEA.

ρ (m^{-2})	γ_{GB} (J/m^2)	S_v (μm^{-1})	E_ρ (MJ/m^3)	E_b (MJ/m^3)
3.5×10^{14}	0.52	0.79	0.90	0.41

recrystallization temperature and thermal stability of the L-PBF CoCrFeMnNi HEA.

5. Conclusions

CoCrFeMnNi HEA was additively manufactured by the L-PBF process. We performed isochronal annealing to study the thermal stability of the AM CoCrFeMnNi HEA. Microstructural evolution at different annealing temperatures was investigated by SXRD, EBSD, and TEM analyses. Thermodynamic calculation of the stored energy and kinetic measurement of the activation energy of recrystallization were carried out to help understand the thermal stability. The main conclusions are drawn as follows:

(1) The as-printed CoCrFeMnNi HEA comprises cellular dislocation structures decorated by a small amount of nanoscale Mn-rich oxides at the cell walls. A total dislocation density of 3.5×10^{14} m^{-2} is measured. The crystallographic misorientations across cell

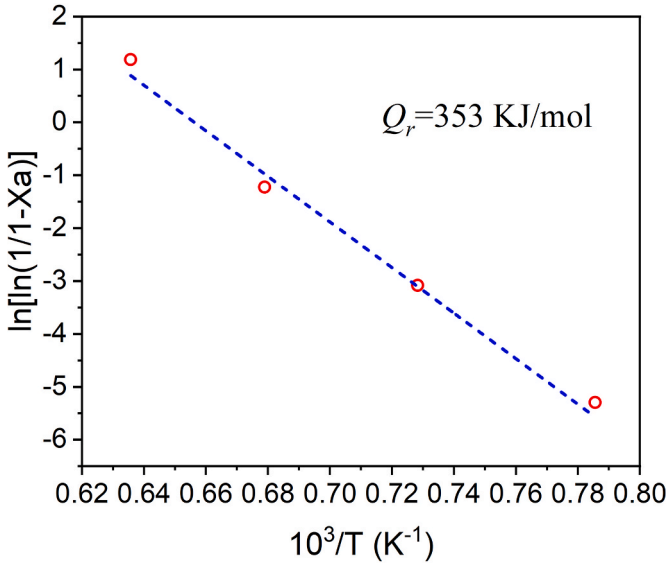

Fig. 9. Arrhenius plot of $ln\,[ln\,(1/1-X_a)]$ versus $1/T$, from which the activation energy for recrystallization of the L-PBF CoCrFeMnNi HEA can be derived as 353 kJ/mol.

walls are very low, leading to the low driving force for recovery and recrystallization.

(2) The activation energy for recrystallization of the L-PBF CoCrFeMnNi HEA was calculated to be 353 kJ/mol. The low driving force for recovery and recrystallization, solute drag, and nanoparticle pinning effects collectively retard dislocation slip and grain boundary migration, resulting in exceptional thermal stability of the L-PBF CoCrFeMnNi HEA.

(3) The cellular dislocation structures are essentially unchanged after annealing at 500 °C for 1 h. The cell walls gradually disappear with increasing the annealing temperature from 700 to 1100 °C, but the majority of LAGBs remain stable. The decomposition and reconfiguration of the cellular structures in the recovery stage significantly retard the recrystallization process, and thus enhance the recrystallization temperature to the regime above 900 °C.

CRediT authorship contribution statement

Yanfang Liu: Methodology, Data curation, Writing – original draft, Writing – review & editing. **Jie Ren:** Data curation. **Jian Liu:** Data curation. **Yang Cao:** Supervision, Writing – review & editing. **Wei Liu:** Supervision. **Tianyi Li:** Data curation. **Yuntian Zhu:** Writing – review & editing. **Wen Chen:** Supervision, Writing – review & editing.

Declaration of competing interest

The authors declare that they have no known competing financial interests or personal relationships that could have appeared to influence the work reported in this paper.

Data availability

Data will be made available on request.

Acknowledgements

W. Chen acknowledges the support from National Science Foundation (DMR-2004429) and UMass Amherst Faculty Startup Fund. Y. Liu acknowledges the support from the Natural Science Foundation of Jiangsu Province (Grants No. BK20220962) and the Open Research Fund of Anhui Key Laboratory of High-Performance Non-ferrous Metal Materials (No. YSJS-2023-05). We acknowledge the experimental support from Jiangsu Key Laboratory of Advanced Micro & Nano Materials and Technology, and the Materials Characterization Center of Nanjing University of Science and Technology. Synchrotron high-energy X-ray diffraction work was carried out at the Advanced Photon Source (Beamline 11-ID-C), which is a US DOE user facility at Argonne National Laboratory.

References

[1] Y.M. Wang, T. Voisin, J.T. McKeown, J. Ye, N.P. Calta, Z. Li, Z. Zeng, Y. Zhang, W. Chen, T.T. Roehling, R.T. Ott, M.K. Santala, Philip J. Depond, M.J. Matthews, A. V. Hamza, T. Zhu, Additively manufactured hierarchical stainless steels with high strength and ductility, Nat. Mater. 17 (1) (2018) 63–71.

[2] Z.G. Zhu, Q.B. Nguyen, F.L. Ng, X.H. An, X.Z. Liao, P.K. Liaw, S.M.L. Nai, J. Wei, Hierarchical microstructure and strengthening mechanisms of a CoCrFeNiMn high entropy alloy additively manufactured by selective laser melting, Scripta Mater. 154 (2018) 20–24.

[3] T. Voisin, J.-B. Forien, A. Perron, S. Aubry, N. Bertin, A. Samanta, A. Baker, Y. M. Wang, New insights on cellular structures strengthening mechanisms and thermal stability of an austenitic stainless steel fabricated by laser powder-bed-fusion, Acta Mater. 203 (2021), 116476.

[4] H. Wang, Z.G. Zhu, H. Chen, A.G. Wang, J.Q. Liu, H.W. Liu, R.K. Zheng, S.M.L. Nai, S. Primig, S.S. Babu, S.P. Ringer, X.Z. Liao, Effect of cyclic rapid thermal loadings on the microstructural evolution of a CrMnFeCoNi high-entropy alloy manufactured by selective laser melting, Acta Mater. 196 (2020) 609–625.

[5] W. Chen, T. Voisin, Y. Zhang, J.B. Florien, C.M. Spadaccini, D.L. McDowell, T. Zhu, Y.M. Wang, Microscale residual stresses in additively manufactured stainless steel, Nat. Commun. 10 (1) (2019) 4338.

[6] Y. Liu, J. Ren, S. Guan, C. Li, Y. Zhang, S. Muskeri, Z. Liu, D. Yu, Y. Chen, K. An, Y. Cao, W. Liu, Y. Zhu, W. Chen, S. Mukherjee, T. Zhu, W. Chen, Microstructure and mechanical behavior of additively manufactured CoCrFeMnNi high-entropy alloys: laser directed energy deposition versus powder bed fusion*, Acta Mater. 250 (2023), 118884.

[7] Y. Cao, S. Ni, X. Liao, M. Song, Y. Zhu, Structural evolutions of metallic materials processed by severe plastic deformation, Mater. Sci. Eng. R 133 (2018) 1–59.

[8] Z. Li, Y. Cui, W. Yan, D. Zhang, Y. Fang, Y. Chen, Q. Yu, G. Wang, H. Ouyang, C. Fan, Q. Guo, D.-B. Xiong, S. Jin, G. Sha, N. Ghoniem, Z. Zhang, Y.M. Wang, Enhanced strengthening and hardening via self-stabilized dislocation network in additively manufactured metals, Mater. Today 50 (2021) 79–88.

[9] L. Liu, Q. Ding, Y. Zhong, J. Zou, J. Wu, Y.-L. Chiu, J. Li, Z. Zhang, Q. Yu, Z. Shen, Dislocation network in additive manufactured steel breaks strength–ductility trade-off, Mater. Today 21 (4) (2018) 354–361.

[10] J. Ren, Y. Zhang, D. Zhao, Y. Chen, S. Guan, Y. Liu, L. Liu, S. Peng, F. Kong, J. D. Poplawsky, G. Gao, T. Voisin, K. An, Y.M. Wang, K.Y. Xie, T. Zhu, W. Chen, Strong yet ductile nanolamellar high-entropy alloys by additive manufacturing, Nature 608 (2022) 62–68.

[11] W. Li, S. Li, J. Liu, A. Zhang, Y. Zhou, Q. Wei, C. Yan, Y. Shi, Effect of heat treatment on AlSi10Mg alloy fabricated by selective laser melting: microstructure evolution, mechanical properties and fracture mechanism, Mater. Sci. Eng., A 663 (2016) 116–125.

[12] K.V. Yang, Y. Shi, F. Palm, X. Wu, P. Rometsch, Columnar to equiaxed transition in Al-Mg(-Sc)-Zr alloys produced by selective laser melting, Scripta Mater. 145 (2018) 113–117.

[13] H. Rao, S. Giet, K. Yang, X. Wu, C.H.J. Davies, The influence of processing parameters on aluminium alloy A357 manufactured by Selective Laser Melting, Mater. Des. 109 (2016) 334–346.

[14] Y.J. Liang, L. Wang, Y. Wen, B. Cheng, Q. Wu, T. Cao, Q. Xiao, Y. Xue, G. Sha, Y. Wang, Y. Ren, X. Li, L. Wang, F. Wang, H. Cai, High-content ductile coherent nanoprecipitates achieve ultrastrong high-entropy alloys, Nat. Commun. 9 (1) (2018) 4063.

[15] B. Gludovatz, A. Hohenwarter, D. Catoor, E.H. Chang, E.P. George, R.O. Ritchie, A fracture-resistant high-entropy alloy for cryogenic applications, Science 345 (6201) (2014) 1153–1158.

[16] W. Jiang, S. Yuan, Y. Cao, Y. Zhang, Y. Zhao, Mechanical properties and deformation mechanisms of a Ni2Co1Fe1V0.5Mo0.2 medium-entropy alloy at elevated temperatures, Acta Mater. 213 (2021) 116982.

[17] B. Xiao, J. Luan, S. Zhao, L. Zhang, S. Chen, Y. Zhao, L. Xu, C.T. Liu, J.J. Kai, T. Yang, Achieving thermally stable nanoparticles in chemically complex alloys via controllable sluggish lattice diffusion, Nat. Commun. 13 (1) (2022) 4870.

[18] M. Shahryar, C. Wen, A review on high-throughput development of high-entropy alloys by combinatorial methods, J. Mater. Inform. 3 (1) (2023) 4.

[19] H. Shahmir, J. He, Z. Lu, M. Kawasaki, T.G. Langdon, Effect of annealing on mechanical properties of a nanocrystalline CoCrFeNiMn high-entropy alloy processed by high-pressure torsion, Mater. Sci. Eng., A 676 (2016) 294–303.

[20] L. Jiang, D. Qiao, Z. Cao, C. Lu, M. Song, L. Wang, Tunable mechanical property and strain hardening behavior of a single-phase CoFeNi2V0.5Mo0.2 high entropy alloy, Mater. Sci. Eng., A 776 (2020) 139027.

[21] K. Ming, L. Li, Z. Li, X. Bi, J. Wang, Grain boundary decohesion by nanoclustering Ni and Cr separately in CrMnFeCoNi high-entropy alloys, Sci. Adv. 5 (12) (2019), eaay0639.

[22] D. Kong, C. Dong, S. Wei, X. Ni, L. Zhang, R. Li, L. Wang, C. Man, X. Li, About metastable cellular structure in additively manufactured austenitic stainless steels, Addit. Manuf. 38 (2021), 101804.

[23] B. Cantor, I.T.H. Chang, P. Knight, A.J.B. Vincent, Microstructural development in equiatomic multicomponent alloys, Mater. Sci. Eng., A 375–377 (2004) 213–218.

[24] G. Laplanche, A. Kostka, O.M. Horst, G. Eggeler, E.P. George, Microstructure evolution and critical stress for twinning in the CrMnFeCoNi high-entropy alloy, Acta Mater. 118 (2016) 152–163.

[25] J. Ren, C. Mahajan, L. Liu, D. Follette, W. Chen, S. Mukherjee, Corrosion behavior of selectively laser melted CoCrFeMnNi high entropy alloy, Metals 9 (10) (2019) 1029.

[26] S. Mooraj, J. Dong, K.Y. Xie, W. Chen, Formation of printing defects and their effects on mechanical properties of additively manufactured metal alloys, J. Appl. Phys. 132 (22) (2022), 225108.

[27] M.N. Hasan, Y.F. Liu, X.H. An, J. Gu, M. Song, Y. Cao, Y.S. Li, Y.T. Zhu, X.Z. Liao, Simultaneously enhancing strength and ductility of a high-entropy alloy via gradient hierarchical microstructures, Int. J. Plast. 123 (2019) 178–195.

[28] Y.-K. Kim, J. Choe, K.-A. Lee, Selective laser melted equiatomic CoCrFeMnNi high-entropy alloy: microstructure, anisotropic mechanical response, and multiple strengthening mechanism, J. Alloys Compd. 805 (2019) 680–691.

[29] W. Jiang, Y. Cao, Y. Jiang, Y. Liu, Q. Mao, H. Zhou, X. Liao, Y. Zhao, Effects of nanostructural hierarchy on the hardness and thermal stability of an austenitic stainless steel, J. Mater. Res. Technol. 12 (2021) 376–384.

[30] X. Huang, N. Hansen, N. Tsuji, Hardening by annealing and softening by deformation in nanostructured metals, Science 312 (5771) (2006) 249–251.

[31] F. Otto, N.L. Hanold, E.P. George, Microstructural evolution after thermomechanical processing in an equiatomic, single-phase CoCrFeMnNi high-entropy alloy with special focus on twin boundaries, Intermetallics 54 (2014) 39–48.

[32] H. Shahmir, T. Mousavi, J. He, Z. Lu, M. Kawasaki, T.G. Langdon, Microstructure and properties of a CoCrFeNiMn high-entropy alloy processed by equal-channel angular pressing, Mater. Sci. Eng., A 705 (2017) 411–419.
[33] J. Gu, M. Song, Annealing-induced abnormal hardening in a cold rolled CrMnFeCoNi high entropy alloy, Scripta Mater. 162 (2019) 345–349.
[34] N.N. Liang, R.R. Xu, G.Z. Wu, X.Z. Gao, Y.H. Zhao, High thermal stability of nanocrystalline FeNi2CoMo0.2V0.5 high-entropy alloy by twin boundary and sluggish diffusion, Mater. Sci. Eng., A 848 (2022), 143399.
[35] G.K. Williamson, W.H. Hall, X-ray line broadening from filed aluminium and wolfram, Acta Metall. 1 (1) (1953) 22–31.
[36] F. HajyAkbary, J. Sietsma, A.J. Böttger, M.J. Santofimia, An improved X-ray diffraction analysis method to characterize dislocation density in lath martensitic structures, Mater. Sci. Eng., A 639 (2015) 208–218.
[37] M. Naeem, H. He, S. Harjo, T. Kawasaki, F. Zhang, B. Wang, S. Lan, Z. Wu, Y. Wu, Z. Lu, C.T. Liu, X.-L. Wang, Extremely high dislocation density and deformation pathway of CrMnFeCoNi high entropy alloy at ultralow temperature, Scripta Mater. 188 (2020) 21–25.
[38] Y.-K. Kim, G.-S. Ham, H.S. Kim, K.-A. Lee, High-cycle fatigue and tensile deformation behaviors of coarse-grained equiatomic CoCrFeMnNi high entropy alloy and unexpected hardening behavior during cyclic loading, Intermetallics 111 (2019), 106486.
[39] F.J. Humphreys, M. Hatherly, Chapter 6 - recovery after deformation, in: F. J. Humphreys, M. Hatherly (Eds.), Recrystallization and Related Annealing Phenomena, second ed., Elsevier, Oxford, 2004, pp. 169–213.
[40] F. Otto, A. Dlouhý, K.G. Pradeep, M. Kuběnová, D. Raabe, G. Eggeler, E.P. George, Decomposition of the single-phase high-entropy alloy CrMnFeCoNi after prolonged anneals at intermediate temperatures, Acta Mater. 112 (2016) 40–52.
[41] M. Annasamy, N. Haghdadi, A. Taylor, P. Hodgson, D. Fabijanic, Static recrystallization and grain growth behaviour of Al0.3CoCrFeNi high entropy alloy, Mater. Sci. Eng., A 754 (2019) 282–294.
[42] S. Guan, D. Wan, K. Solberg, F. Berto, T. Welo, T.M. Yue, K.C. Chan, Additive manufacturing of fine-grained and dislocation-populated CrMnFeCoNi high entropy alloy by laser engineered net shaping, Mater. Sci. Eng., A 761 (2019), 138056.
[43] M. Glienke, M. Vaidya, K. Gururaj, L. Daum, B. Tas, L. Rogal, K.G. Pradeep, S. V. Divinski, G. Wilde, Grain boundary diffusion in CoCrFeMnNi high entropy alloy: kinetic hints towards a phase decomposition, Acta Mater. 195 (2020) 304–316.
[44] F.J. Humphreys, M. Hatherly, Recrystallization and Related Annealing Phenomena, Elsevier, 2012.
[45] W.Q. Cao, C.F. Gu, E.V. Pereloma, C.H.J. Davies, Stored energy, vacancies and thermal stability of ultra-fine grained copper, Mater. Sci. Eng., A 492 (1) (2008) 74–79.
[46] A. Godfrey, W.Q. Cao, Q. Liu, N. Hansen, Stored energy, microstructure, and flow stress of deformed metals, Metall. Mater. Trans. A 36 (9) (2005) 2371–2378.
[47] F.J. Humphreys, M. Hatherly, Chapter 4 - the structure and energy of grain boundaries, in: F.J. Humphreys, M. Hatherly (Eds.), Recrystallization and Related Annealing Phenomena, second ed., Elsevier, Oxford, 2004, pp. 91–119.
[48] F.J. Humphreys, M. Hatherly, Chapter 2 - the deformed state, in: F.J. Humphreys, M. Hatherly (Eds.), Recrystallization and Related Annealing Phenomena, second ed., Elsevier, Oxford, 2004, pp. 11–II.
[49] H.W. Zhang, X. Huang, R. Pippan, N. Hansen, Thermal behavior of Ni (99.967% and 99.5% purity) deformed to an ultra-high strain by high pressure torsion, Acta Mater. 58 (5) (2010) 1698–1707.
[50] F.J. Humphreys, M. Hatherly, Chapter 7 - recrystallization of single-phase alloys, in: F.J. Humphreys, M. Hatherly (Eds.), Recrystallization and Related Annealing Phenomena, second ed., Elsevier, Oxford, 2004, pp. 215–IV.
[51] M. Vaidya, K.G. Pradeep, B.S. Murty, G. Wilde, S.V. Divinski, Bulk tracer diffusion in CoCrFeNi and CoCrFeMnNi high entropy alloys, Acta Mater. 146 (2018) 211–224.
[52] Y. Lü, D.A. Molodov, G. Gottstein, Recrystallization kinetics and microstructure evolution during annealing of a cold-rolled Fe–Mn–C alloy, Acta Mater. 59 (8) (2011) 3229–3243.
[53] F. Cuevas, M. Reis, A. Ferraiuolo, G. Pratolongo, L.P. Karjalainen, V. Navas, J. Gil Sevillano, Kinetics of recrystallization and grain growth of cold rolled TWIP steel, Adv. Mater. Res. 89 (2010) 153–158.
[54] K.Y. Tsai, M.H. Tsai, J.W. Yeh, Sluggish diffusion in Co–Cr–Fe–Mn–Ni high-entropy alloys, Acta Mater. 61 (13) (2013) 4887–4897.
[55] D. Raabe, 23 - recovery and recrystallization: phenomena, physics, models, simulation, in: D.E. Laughlin, K. Hono (Eds.), Physical Metallurgy, fifth ed., Elsevier, Oxford, 2014, pp. 2291–2397.
[56] M.V. Klimova, D.G. Shaysultanov, S.V. Zherebtsov, N.D. Stepanov, Effect of second phase particles on mechanical properties and grain growth in a CoCrFeMnNi high entropy alloy, Mater. Sci. Eng., A 748 (2019) 228–235.
[57] W.Q. Cao, C.F. Gu, E.V. Pereloma, C.H.J. Davies, Stored energy, vacancies and thermal stability of ultra-fine grained copper, Mater. Sci. Eng., A 492 (1–2) (2008) 74–79.
[58] X.L. Wu, M.X. Yang, F.P. Yuan, L. Chen, Y.T. Zhu, Combining gradient structure and TRIP effect to produce austenite stainless steel with high strength and ductility, Acta Mater. 112 (2016) 337–346.